Susceptibility of F/A-18 Flight Control Laws to the Falling Leaf Mode
Part II: Nonlinear Analysis

Abhijit Chakraborty *, Peter Seiler † and Gary J. Balas‡

Department of Aerospace Engineering & Mechanics University of Minnesota , Minneapolis, MN, 55455, USA

The F/A-18 Hornet aircraft with the original flight control law exhibited an out-of-control phenomenon known as the falling leaf mode. The falling leaf mode went undetected during the validation and verification stage of the flight control law. Several F/A-18 Hornet aircraft were lost due to the falling leaf mode which led to the redesign of the lateral-directional axis of the flight control law. The revised flight control law exhibited successful suppression of the falling leaf mode during flight tests with aggressive maneuvers. Prior to performing expensive flight tests, the flight control law was extensively validated and verified by performing linear robustness analysis at different trim points and running many Monte-Carlo simulations. Additional insight can be gained by using nonlinear analyses. This paper compares the two flight control laws using nonlinear region-of-attraction analyses and Monte Carlo simulations. The results of these nonlinear analyses indicate that the revised flight control law has better significantly improved nonlinear robustness properties as compared with baseline design.

Nomenclature

α Angle-of-attack, *rad*

β Sideslip Angle, *rad*

V Velocity, $\frac{ft}{s}$

p Roll rate, $\frac{rad}{s}$

q Pitch rate, $\frac{rad}{s}$

r Yaw rate, $\frac{rad}{s}$

ϕ Bank angle, *rad*

θ Pitch angle, *rad*

---

*Graduate Research Assistant: chakrab@aem.umn.edu.

†Senior Research Associate: seiler@aem.umn.edu.

‡Professor: balas@aem.umn.edu.

American Institute of Aeronautics and Astronautics

ψ	Yaw angle, rad	
T	Thrust, lbf	
ρ	Density, $\frac{slugs}{ft^3}$	
$\bar{q}$	Dynamic pressure, $\frac{lbs}{ft^2}$	
m	Mass, $slugs$	
g	Gravitational Constant, $\frac{ft}{s^2}$	
a_y	Lateral acceleration, g	
$I.C.$	Initial Condition	

I. Introduction

Safety critical flight systems require extensive validation prior to entry into service. Validation of the flight control system is becoming more difficult due to the increased use of advanced flight control algorithms, e.g. nonlinear flight controls systems. NASA's Aviation Safety Program (AvSP) aims to reduce the fatal (commercial) aircraft accident rate by 90% by 2022.[1] A key challenge to achieving this goal is the need for extensive validation and certification tools for the flight systems. The current certification and validation procedure involves analysis, simulations, and experimental techniques such as flight tests.[1] Prior to flight tests, extensive analyses and simulations are performed to validate safety of the system. Standard practice is to assess the closed-loop stability and performance characteristics of the aircraft flight control system around numerous trim conditions using linear analysis tools. These techniques include stability margins, robustness analyses and worst-case analyses. These linear analyses are supplemented with Monte Carlo simulations of the full nonlinear equations of motion to provide further confidence in the system performance.

The simulations are also used to uncover nonlinear dynamic characteristics, e.g. limit cycles, that are not revealed by the linear analyses. Hence, current practice involves extensive linear analyses at different trim conditions and probabilistic nonlinear simulations. The certification process typically does not involve nonlinear analysis methods. This gap between linear analyses and Monte Carlo simulations can result in significant nonlinear effects going undetected. The F/A-18 Hornet aircraft is one example which suffered from the existing gap in the validation procedure.

The US Navy F/A-18 A/B/C/D Hornet aircraft with the original baseline flight control law experienced a number of out-of-control flight departures since the early 1980's. Many of these incidents have been described as a falling leaf motion of the aircraft.[2] The falling leaf motion dynamics is nonlinear in nature which made analysis challenging. An extensive revision of the baseline control law was performed by NAVAIR and Boeing in 2001 to suppress departure phenomenon, improve maneuvering performance and to expand the flight envelope.[2] The revised control law was implemented on the F/A-18 E/F Super Hornet aircraft after successful flight tests. These flight tests included aggressive maneuvers that demonstrated successful suppression of the falling leaf motion by the revised control law.

The baseline flight control law of the F/A-18 Hornet aircraft went through the extensive validation and verification process without detecting the susceptibility to the falling leaf motion. The failure to detect the falling leaf motion is not due to the lack of an accurate aerodynamic model. In fact, it was shown[3] that a nonlinear simulation model of the F/A-18 Hornet aircraft is able to reproduce the falling leaf mode. Thus the failure to detect this susceptibility must be attributed to the lack of appropriate analysis tools.

Classical gain and phase margin analyses indicate that the revised flight control law has similar robustness properties as the baseline flight control law.[3] More advanced linear analysis tools, such as μ and worst-case performance, indicate that the revised flight controller has noticeably better robustness properties than the baseline control law.[3] However, it can be difficult to interpret these results since the falling leaf motion is a truly nonlinear dynamical phenomenon. Thus nonlinear analyses tools would provide useful insight into the susceptibility of both control laws to the falling leaf motion.

Recently, significant research has been performed on the development of nonlinear analysis tools for computing regions of attraction, reachability sets, input-output gains, and robustness with respect to uncertainty for nonlinear polynomial systems.[4–13] These tools make use of polynomial sum-of-squares optimization[13] and hence they can only be applied to systems whose dynamics are described by polynomial vector fields. These techniques offer great potential to complement the linear analyses and nonlinear simulations that are typically used in the flight control validation process.

The main objective of this paper is to use Monte Carlo simulations and nonlinear region of attraction analyses to assess the robustness properties of the two F/A-18 flight control laws. Region of attraction (ROA) analysis for nonlinear systems provides a guaranteed stability region using Lyapunov theory and sum-of-squares optimization.[4–6, 13, 14] The ROA analysis complements the use of Monte Carlo simulations. Sum-of-squares stability analysis has previously been applied to simple examples.[4–6, 13, 14] This paper presents the first successful application of these techniques to an actual industrial flight control problem. The falling leaf motion is due to nonlinearities in the aircraft dynamics and cannot be replicated with linear models. Thus analysis of the F/A-18 control laws is a particularly interesting example for the application of nonlinear robustness analysis techniques.

The paper has the following structure. First, a computational procedure to estimate regions of attraction for polynomial systems[4–6, 15–18] is provided in Section II. The six degree-of-freedom (DOF) nine state model of the F/A-18 aircraft is discussed in Section III. State-space realizations for the baseline and revised control laws are given in Section IV. Polynomial models are constructed in Section V for the closed loop systems with the baseline and revised flight control laws. This step is required because the computational method to estimate the ROA is only applicable for polynomial systems. The robustness properties of the two closed-loop systems are then analyzed in Section VI. The paper concludes with a summary of the contributions of the paper.

II.   Region-of-Attraction (ROA) Estimation

This section describes the technical approach to estimate the region of attraction for nonlinear, polynomial systems. This analysis is based on a fundamental difference between asymptotic stability for linear and nonlinear systems. For linear systems, asymptotic stability of an equilibrium point is a global property. In other words, if an equilibrium point is asymptotically stable then its state trajectory will converge back to the equilibrium when starting from any initial condition. For nonlinear systems, asymptotically stable equilibrium points are not necessarily globally asymptotically stable. Khalil[19] and Vidyasagar[20] provide good introductory discussions of this issue. The region-of-attraction (ROA) of an asymptotically stable equilibrium point is the set of initial conditions whose state trajectories converge back to the equilibrium.[19] If the ROA is small, then a disturbance can easily drive the system out of the ROA and the system will fail to come back to the stable equilibrium point. Thus the size of the ROA can be interpreted as a measure of the stability properties of a nonlinear system around an equilibrium point. This motivates the computation of ROA estimates.

Consider an autonomous nonlinear, polynomial system of the form:

$$\dot{x} = f(x), \ x(0) = x_0 \tag{1}$$

where $x \in \mathbb{R}^n$ is the state vector and $f : \mathbb{R}^n \to \mathbb{R}^n$ is a multivariable polynomial. Assume that the origin is a locally asymptotically stable equilibrium point. This assumption is without loss of generality because state coordinates can always be redefined to shift an equilibrium point to the origin. The ROA is formally defined as:

$$\mathcal{R} := \left\{ x_0 \in \mathbb{R}^n : \text{ If } x(0) = x_0 \text{ then } \lim_{t \to \infty} x(t) = 0 \right\} \tag{2}$$

Computing the exact ROA for nonlinear dynamical systems is very difficult. There has been significant research devoted to estimating invariant subsets of the ROA.[7–13, 21, 22] The approach taken in this paper is to restrict the search to ellipsoidal approximations of the ROA. Given an $n \times n$ matrix $N = N^T > 0$, define the shape function $p(x) := x^T N x$ and level set $\mathcal{E}_\beta := \{ x \in \mathbb{R}^n : p(x) \leq \beta \}$. $p(x)$ defines the shape of the ellipsoid and β determines the size of the ellipsoid $\mathcal{E}_\beta$. The choice of p is problem dependent and reflects dimensional scaling information as well as the importance of certain directions in the state space. N can typically be chosen to be diagonal with $N_{i,i} := 1/x_{i,max}^2$. With this choice, $\mathcal{E}_{\beta=1}$ is a coordinate-aligned ellipsoid whose extreme points along the ith state direction are $\pm x_{i,max}$. In this form, the level set value β provides an easily interpretable value for the size of the level set.

Given the shape function p, the problem is to find the largest ellipsoid $\mathcal{E}_\beta$ contained in the ROA:

$$\beta^* = \max \beta \tag{3}$$

$$\text{subject to: } \mathcal{E}_\beta \subset \mathcal{R}$$

Determining the best ellipsoidal approximation to the ROA is still a challenging computational problem.

American Institute of Aeronautics and Astronautics

Instead, lower and upper bounds for β^* satisfying $\underline{\beta} \leq \beta^* \leq \bar{\beta}$ are computed. If the lower and upper bounds are close then the largest ellipsoid level set, defined by Equation (3), has been approximately computed.

The upper bounds are computed via a search for initial conditions leading to divergent trajectories. If $\lim_{t\to\infty} x(t) = +\infty$ when starting from $x(0) = x_{0,div}$ then $x_{0,div} \notin \mathcal{R}$. If we define $\bar{\beta}_{div} := p(x_{0,div})$ then $\mathcal{E}_{\bar{\beta}_{div}} \not\subset \mathcal{R}$ which implies $\beta^* \leq \bar{\beta}_{div}$. An exhaustive Monte Carlo search is used to find a tight upper bound on β^*. Specifically, random initial conditions are chosen starting on the boundary of a large ellipsoid: x_0 is chosen to satisfy $p(x_0) = \beta_{try}$ where β_{try} is sufficiently large that $\beta_{try} \gg \beta^*$. If a divergent trajectory is found, the initial condition is stored and an upper bound on β^* is computed. β_{try} is then decreased by a factor of 0.995 and the search continues until a maximum number of simulations is reached. There is a trade-off involved in choosing the factor 0.995. A smaller factor results in a larger reduction of the upper bound for each divergent trajectory but it typically limits the accuracy of the upper bound. No divergent trajectories can be found when $\beta_{try} < \beta^*$ and this roughly limits the upper bound accuracy to $\beta^*/(\text{factor})$. The value of 0.995 is very close to one and is chosen to obtain an accurate upper bound on β^*. $\bar{\beta}_{MC}$ will denote the smallest upper bound computed with this Monte Carlo search.

The lower bounds are computed using Lyapunov functions and recent results connecting sums-of-squares polynomials to semidefinite programming. Computing these bounds requires the vector field $f(x)$ in Equation (1) to be a polynomial function. The computational algorithm is briefly described here and full algorithmic details are provided in references.[4–6, 15–18] Lemma 1 is the main Lyapunov theorem used to compute lower bounds on β^*. This specific lemma is proved by[4] but very similar results are given in textbooks.[20]

Lemma 1 *If there exists $\gamma > 0$ and a polynomial $V : \mathbb{R}^n \to \mathbb{R}$ such that:*

$$V(0) = 0 \ and \ V(x) > 0 \ \forall x \neq 0 \tag{4}$$

$$\Omega_\gamma := \{x \in \mathbb{R}^n \ : \ V(x) \leq \gamma\} \ is \ bounded. \tag{5}$$

$$\Omega_\gamma \subset \{x \in \mathbb{R}^n \ : \ \nabla V(x) f(x) < 0\} \cup \{0\} \tag{6}$$

then for all $x \in \Omega_\gamma$, the solution of Equation (1) exists, satisfies $x(t) \in \Omega_\gamma$ for all $t \geq 0$, and $\Omega_\gamma \subset \mathcal{R}$.

A function V, satisfying the conditions in Lemma 1 is a Lyapunov function and Ω_γ provides an estimate of the region of attraction. If $x = 0$ is asymptotically stable, a linearization can be used to compute a Lyapunov function. Let $A := \frac{\partial f}{\partial x}\big|_{x=0}$ be the linearization of the dynamics about the origin and compute $P > 0$ that solves the Lyapunov equation $A^T P + PA = -I$. $V_{LIN}(x) := x^T P x$ is a quadratic Lyapunov function that satisfies the conditions of Lemma 1 for sufficiently small $\gamma > 0$. V_{LIN} can be used to compute a lower bound

on β^* by solving two maximizations:

$$\gamma^* := \max \gamma \tag{7}$$
$$\text{subject to: } \Omega_\gamma \subset \{x \in \mathbb{R}^n \ : \ \nabla V_{LIN}(x)f(x) < 0\}$$

$$\underline{\beta} := \max \beta \tag{8}$$
$$\text{subject to: } \mathcal{E}_\beta \subset \Omega_{\gamma^*}$$

The first maximization finds the largest level set Ω_{γ^*} of V_{LIN} such that Lemma 1 can be used to verify $\Omega_{\gamma^*} \subseteq \mathcal{R}$. The second maximization finds the largest ellipsoid $\mathcal{E}_{\underline{\beta}}$ contain within Ω_{γ^*}. The set containment constraints are replaced with a sufficient condition involving non-negative polynomials.[4] For example, $\mathcal{E}_\beta \subset \Omega_{\gamma^*}$ in Optimization (8) is replaced by

$$\underline{\beta} := \max_{\beta, \ s(x)} \beta \tag{9}$$
$$\text{subject to: } s(x) \geq 0 \ \forall x$$
$$- (\beta - p(x)) \, s(x) + (\gamma^* - V_{LIN}(x)) \geq 0 \ \forall x$$

The function $s(x)$ is a decision variable of the optimization, i.e. it is found as part of the optimization. It is straight-forward to show that the two non-negativity conditions in Optimization (9) are a sufficient condition for the set containment condition in Optimization (8). If $s(x)$ is restricted to be a polynomial, both constraints involve the non-negativity of polynomial functions. A sufficient condition for a generic multi-variate polynomial $h(x)$ to be non-negative is the existence of polynomials $\{g_1, \ldots, g_n\}$ such that $h = g_1^2 + \cdots + g_n^2$. A polynomial which can be decomposed in this way is called a sum-of-squares (SOS). Finally, if we replace the non-negativity conditions in Optimization (9) with SOS constraints, then we arrive at an SOS optimization problem:

$$\underline{\beta} := \max \beta \tag{10}$$
$$\text{subject to: } s(x) \text{ is SOS}$$
$$- (\beta - p(x))s(x) + (\gamma^* - V_{LIN}(x)) \text{ is SOS}$$

There are connections between SOS polynomials and semidefinite matrices. Moreover, optimization problems involving SOS constraints can be converted and solved as a semidefinite programming optimization. Importantly, there is freely available software to set up and solve these problems.[14, 23–25] $\underline{\beta}_{LIN}$ will denote the lower bound obtained from Optimization (10) using the quadratic Lyapunov function obtained from linearized analysis.

Unfortunately, $\underline{\beta}_{LIN}$ is usually orders of magnitude smaller than the upper bound $\bar{\beta}_{MC}$. Several methods

American Institute of Aeronautics and Astronautics

to compute better Lyapunov functions exist, including V-s iterations,[15–18] bilinear optimization,[4] and the use of simulation data.[5,6] In this paper, V-s iteration is used to compute the Lyapunov function and the inner ellipsoidal approximation to the ROA. The Lyapunov function $V(x)$ in the iteration is initialized with the linearized Lyapunov function V_{LIN}. The iteration also uses functions $l_1(x) = -\epsilon_1 x^T x$ and $l_2(x) = -\epsilon_2 x^T x$ where ϵ_1 and ϵ_2 are small positive constants on the order of 10^{-6}. The V-s iteration algorithm steps are:

1. γ **Step**: Hold V fixed and solve for s_2 and γ^*

$$\gamma^* := \max_{s_2 \in \text{SOS}, \gamma} \gamma \quad \text{s.t.} \quad -(\gamma - V)s_2 - \left(\frac{\partial V}{\partial x}f + l_2\right) \in \text{SOS}$$

2. β **Step**: Hold V, γ^* fixed and solve for s_1 and $\underline{\beta}$

$$\underline{\beta} := \max_{s_1 \in \text{SOS}, \beta} \beta \quad \text{s.t.} \quad -(\beta - p)s_1 + (\gamma^* - V) \in \text{SOS}$$

3. V **step**: Hold s_1, s_2, $\underline{\beta}$, γ^* fixed and solve for V satisfying:

$$-(\gamma^* - V)s_2 - \left(\frac{\partial V}{\partial x}f + l_2\right) \in \text{SOS}$$
$$-(\underline{\beta} - p)s_1 + (\gamma^* - V) \in \text{SOS}$$
$$V - l_1 \in \text{SOS}, V(0) = 0$$

4. Repeat as long as the lower bound $\underline{\beta}$ continues to increase.

Software and additional documentation on the V-s iteration is provided in the references.[25] The basic issue is that searching for a Lyapunov function V results in a bilinear term Vs_2 in the γ constraint. This bilinear term can not be handled directly within the SOS programming framework because the constraints in SOS programs must be linear in the decision variables. The $V - s$ iteration avoids the bilinearity in Vs_2 by holding either s_2 or V fixed. Each step of this iteration is a linear SOS optimization that can be solved with available software. In the V-s iteration, the Lyapunov functions are allowed to have polynomial degree greater than two. Increasing the degree of the Lyapunov function will improve the lower bound at the expense of computational complexity.

The V step requires additional discussion. An interior-point linear matrix inequality solver is used to find a feasible solution to the feasibility problem in the V step. The Lyapunov function V that is used in the γ and β steps will be feasible for the constraints in the V step. Thus it is possible for the solver to simply return the same Lyapunov function that was used in the γ and β steps. While this is possible, it typically happens that the solver returns a different V that allows both γ and β to be increased at the next iteration. This step can be understood by the fact that interior point solvers try to return a solution at the analytic center of set specified by the linear matrix inequality constraints. Thus the V step typically returns a feasible V that is "pushed away" from the constraints. A more formal theory for the behavior of this feasibility step is an open question.

III. F/A-18 Aircraft and Model Development

This section provides a brief mathematical description of the six degree-of-freedom (DOF) F/A-18 aircraft. A more detailed description can be found in[3] and the references therein. It is important to note that the falling leaf motion can be reproduced in simulation using this six DOF model of the F/A-18 aircraft.[3]

The mathematical description of the DOF, 9-state model for the F/A-18 aircraft uses flight tests data publicly available for the F/A-18 High Alpha Research Vehicle (HARV).[26–30] The aerodynamic characteristics of the F/A-18 Hornet and Super Hornet are similar to the HARV aircraft. The aerodynamic characteristics of the aircraft are expressed as closed-form polynomial approximations to flight test data with functional dependence on states and control surfaces.[3] State variables describing the F/A-18 mathematical model are: velocity (V, ft/s), sideslip angle (β, rad), angle-of-attack (α, rad), roll rate (p, rad/s), pitch rate (q, rad/s), yaw rate (r, rad/s), bank angle (ϕ, rad), pitch angle (θ, rad) and yaw angle (ψ, rad). Symmetric stabilator (δ_{stab}, rad), differential aileron (δ_{ail}, rad), differential rudder (δ_{rud}, rad) and thrust (T, lbf) are considered as control effectors for the analyses performed in this paper. Table 1 lists the aerodynamic reference and physical parameters of the F/A-18 Hornet.[31]

Table 1. Aircraft Parameters

Wing Area, S	400 ft^2
Mean Aerodynamic Chord, $\bar{c}$	11.52 ft
Wing Span, b	37.42 ft
Mass, m	1034.5 slugs
Roll Axis Moment of Inertia, I$_{xx}$	23000 slug-ft^2
Pitch Axis Moment of Inertia, I$_{yy}$	151293 slug-ft^2
Yaw Axis Moment of Inertia, I$_{zz}$	169945 slug-ft^2
Cross-product of Inertia about y-axis, I$_{xz}$	-2971 slug-ft^2

The mathematical model of the F/A-18 Hornet is described by the conventional aircraft equations of motion[30, 32, 33] in the following form:

$$\dot{x} = f(x, u) \tag{11}$$

where $x := [V(\text{ft/s}), \ \beta(\text{rad}), \ \alpha(\text{rad}), \ p(\text{rad/s}), \ q(\text{rad/s}) \ r(\text{rad/s}), \ \phi(\text{rad}), \ \theta(\text{rad}), \ \psi(\text{rad})]$. and $u := [\delta_{ail}(\text{rad}), \ \delta_{rud}(\text{rad}), \ \delta_{stab}(\text{rad}), \ T(\text{lbf})]$.

The equations of motion are presented next. Closed-form polynomial expressions for the aerodynamic coefficients are presented in Appendix A. A detailed description of the aerodynamic model is provided in.[3]

The kinematics of the aircraft are described in terms of Euler angles. The kinematic relations are given in Equation (12).

$$\begin{bmatrix} \dot{\phi} \\ \dot{\theta} \\ \dot{\psi} \end{bmatrix} = \begin{bmatrix} 1 & \sin\phi\tan\theta & \cos\phi\tan\theta \\ 0 & \cos\phi & -\sin\phi \\ 0 & \sin\phi\sec\theta & \cos\phi\sec\theta \end{bmatrix} \begin{bmatrix} p \\ q \\ r \end{bmatrix} \tag{12}$$

American Institute of Aeronautics and Astronautics

Equation (13) defines the force equations for the F/A-18 Hornet. The aerodynamic forces, gravity forces and thrust force applied to the aircraft are considered. For all analyses, the thrust force is assumed to be constant and fixed at its trim value.

$$\dot{V} = -\frac{1}{m}(D\cos\beta - Y\sin\beta) + g(\cos\phi\cos\theta\sin\alpha\cos\beta + \sin\phi\cos\theta\sin\beta$$
$$- \sin\theta\cos\alpha\cos\beta) + \frac{T}{m}\cos\alpha\cos\beta \tag{13a}$$

$$\dot{\alpha} = -\frac{1}{mV\cos\beta}L + q - \tan\beta(p\cos\alpha + r\sin\alpha)$$
$$+ \frac{g}{V\cos\beta}(\cos\phi\cos\theta\cos\alpha + \sin\alpha\sin\theta) - \frac{T\sin\alpha}{mV\cos\beta} \tag{13b}$$

$$\dot{\beta} = \frac{1}{mV}(Y\cos\beta + D\sin\beta) + p\sin\alpha - r\cos\alpha + \frac{g}{V}\cos\beta\sin\phi\cos\theta$$
$$+ \frac{\sin\beta}{V}(g\cos\alpha\sin\theta - g\sin\alpha\cos\phi\cos\theta + \frac{T}{m}\cos\alpha) \tag{13c}$$

where C_D, C_L, C_Y denote the drag, lift and sideforce coefficients, respectively. These force coefficients are expressed as a sum of basic airframe and control deflections as $C_* = C_{*,basic}(\alpha,\beta) + C_{*,control}(\alpha,\delta_{control})$. The variable '*' denotes D, L, Y and $\delta_{control}$ can be replaced by δ_{stab}, δ_{ail}, δ_{rud}. The detailed expressions for these force coefficients are provided in Appendix A.

The aerodynamic moments are considered for external applied moments. The gyroscopic effect of the moment is neglected in this paper. Equation (14) describes the moment equations for the F/A-18 Hornet.

$$\begin{bmatrix} \dot{p} \\ \dot{q} \\ \dot{r} \end{bmatrix} = \begin{bmatrix} \frac{I_{zz}}{\kappa} & 0 & \frac{I_{xz}}{\kappa} \\ 0 & \frac{1}{I_{yy}} & 0 \\ \frac{I_{xz}}{\kappa} & 0 & \frac{I_{xx}}{\kappa} \end{bmatrix} \left(\begin{bmatrix} l \\ M \\ n \end{bmatrix} - \begin{bmatrix} 0 & -r & q \\ r & 0 & -p \\ -q & p & 0 \end{bmatrix} \begin{bmatrix} I_{xx} & 0 & -I_{xz} \\ 0 & I_{yy} & 0 \\ -I_{xz} & 0 & I_{zz} \end{bmatrix} \begin{bmatrix} p \\ q \\ r \end{bmatrix} \right) \tag{14}$$

where $\kappa = I_{xx}I_{zz} - I_{xz}^2$. $l := \bar{q}SbC_l$, $M := \bar{q}ScC_M$, $n := \bar{q}SbC_n$ denote the roll, pitch and yaw moment, respectively. The moment coefficients, C_l, C_M, and C_n, are expressed as a sum of basic airframe, control deflections, and rate damping as $C_* = C_{*,basic}(\alpha,\beta) + C_{*,control}(\alpha,\delta_{control}) + C_{*,rate}(rate,V)$. The variable '*' denotes l, M, n , control denotes stab, ail, rud and rate denotes the variable p, q, r. Appendix A provides explicit forms for these moment coefficients.

IV.   F/A-18 Flight Control Laws

State-space realizations for both the baseline and revised flight control laws are presented in this section. A simplified architecture for the flight control laws is used to formulate the state-space realization. More detailed descriptions of these flight control laws can be found in.[3]

The baseline controller structure for the F/A-18 aircraft closely follows the *Control Augmentation System (CAS)* presented in the report by Buttrill, Arbuckle, and Hoffler.[31] The papers by Heller, David, & Holmberg[2] and Heller, Niewoehner, & Lawson[34] provide a detailed description of the revised flight control

law. The actuator dynamics are neglected in this paper. The actuators have fast dynamics and can be neglected without causing any significant variation in the analysis results.

The controller, $K = \left[\begin{array}{c|c} A_c & B_c \\ \hline C_c & D_C \end{array} \right]$ can be realized as following:

$$\dot{x}_c = A_c x_c + B_c y \tag{15}$$

$$u_3 = C_c x_c + D_c y \tag{16}$$

where x_c is the controller state, $u_3 := [\delta_{ail}, \delta_{rud}, \delta_{stab}]$ indicates the input of the plant. The plant measurements are $y := [a_y, p, r, \alpha, \beta, q, \dot{\beta}_{lin}]$. The lateral acceleration is given by $a_y = \dfrac{\bar{q}S}{mg} C_Y$ (in units of g) and computed around a flight condition. Moreover, the measurement signal $\dot{\beta}_{lin}$ represents the linearized representation of the sideslip-rate ($\dot{\beta}$). This signal is estimated by using a 1st order approximation to the sideslip state derivative equation around a flight condition.

The baseline flight control law is:

$$\left[\begin{array}{c|c} A_c & B_c \\ \hline C_c & D_c \end{array} \right] = \left[\begin{array}{c|ccccccc} -1 & 0 & 0 & 4.9 & 0 & 0 & 0 & 0 \\ \hline 0 & 0 & 0.8 & 0 & 0 & 0 & 0 & 0 \\ -1 & -0.5 & 0 & -1.1 & 0 & 0 & 0 & 0 \\ 0 & 0 & 0 & 0 & -0.8 & 0 & -8 & 0 \end{array} \right] \tag{17}$$

and the revised controller is:

$$\left[\begin{array}{c|c} A_c & B_c \\ \hline C_c & D_c \end{array} \right] = \left[\begin{array}{c|ccccccc} -1 & 0 & 0 & 4.9 & 0 & 0 & 0 & 0 \\ \hline 0 & 0 & 0.8 & 0 & 0 & 2 & 0 & 0.5 \\ -1 & -0.5 & 0 & -1.1 & 0 & 0 & 0 & 0 \\ 0 & 0 & 0 & 0 & -0.8 & 0 & -8 & 0 \end{array} \right] \tag{18}$$

The revised flight control law has two additional feedback channels, sideslip and sideslip rate feedback, compared with the baseline flight control law. The paper by Heller, David, & Holmberg[2] refers to these additional two feedback channels, especially the sideslip rate feedback, being the key for suppressing the falling leaf motion.

V. Polynomial Model Formulation & Validation of F/A-18 Aircraft

Section II described an approach to estimate regions of attraction for nonlinear systems. The approach to estimate lower bounds on the ROA relies on SOS optimization methods and can only be applied to polynomial systems. Moreover, the computational requirements for the SOS optimizations grow rapidly in the number of state variables and polynomial degree. This approximately limits this method to nonlinear

American Institute of Aeronautics and Astronautics

analysis problems with at most 7-10 states and degree 3-5 polynomial models. Consequently, the construction of accurate, low-degree polynomial models is an important step in the proposed analysis process. This section formulates cubic degree polynomial models for the closed-loop systems consisting of the F/A-18 aircraft and the baseline and revised flight control laws.

A. Polynomial Model Formulation

A nine state, six DOF nonlinear model for the F/A-18 was described in Section III. The phugoid mode of the aircraft involves the V and θ states. The phugoid mode is slow and is not important for capturing the falling leaf characteristics. The heading angle ψ also does not impact any of other state dynamics and hence it can be neglected. Consequently a six state model of the F/A-18 aircraft is sufficient for analyzing the falling leaf mode. Additional rationale for neglecting (V, θ, ψ) is discussed in.[3]

The mechanism to extract a six-state representation from the nine-state model is outlined. First, the nine-state model, Equation (11), is trimmed around a specific flight condition. Consider the flight condition for a coordinated turn $(\beta_t = 0^o)$ at a 35° bank angle and at $V_t = 350$ ft/s. The trim values are provided in Equation (19). The subscript 't' denotes a trim value.

$$
\begin{bmatrix} \alpha_t \\ p_t \\ q_t \\ r_t \\ \theta_t \\ \psi_t \end{bmatrix} = \begin{bmatrix} 20.17^o \\ -1.083^o/s \\ 1.855^o/s \\ 2.634^o/s \\ 18.69^0 \\ 0^o \end{bmatrix}, \quad \begin{bmatrix} \delta_{stab,t} \\ \delta_{ail,t} \\ \delta_{rud,t} \\ \delta_{th,t} \end{bmatrix} = \begin{bmatrix} -4.449^o \\ -0.4383^o \\ -1.352^o \\ 14500 \text{ lbf} \end{bmatrix}
\tag{19}
$$

The analysis in this paper, is performed around the flight condition mentioned in Equation (19). This flight condition is one of the eight different operating points, specifically Plant 4, around which linear analysis was performed in a previous work.[3]

The states and inputs for the six-state model are defined relative to this trim point: $x_6 := [\beta - \beta_t, \ \alpha - \alpha_t, \ p - p_t, \ q - q_t, \ r - r_t, \ \phi - \phi_t]$ and $u_3 := [\delta_{ail} - \delta_{ail_t}, \ \delta_{rud} - \delta_{rud_t}, \ \delta_{stab} - \delta_{stab_t}]$. The state derivatives for the six state model, $\dot{x}_6$, are computed using Equation (13c), (13b), (14) and the first row ($\dot{\phi}$ entry) of (12), respectively. In these equations, V, θ, ψ and T are held fixed at their trimmed values. Moreover, these state derivatives are linear in the inputs. Thus the six-state model is of the following form:

$$
\dot{x}_6 = F(x_6) + G(x_6)u_3
\tag{20}
$$

$$
y = H(x_6) + J(x_6)u_3
\tag{21}
$$

Figure 1 shows the structure of the closed-loop plant considered. P denotes the 6-state nonlinear model mentioned in Equation (20) and (21). K denotes either the baseline or revised control law presented in

American Institute of Aeronautics and Astronautics

Section IV. Both the closed-loop models are formed with the negative feedback of the controller (K) around the nonlinear plant (P), as shown in Figure 1.
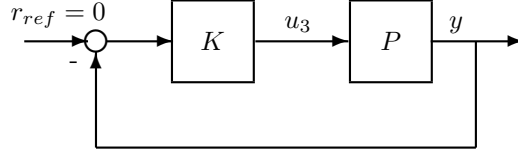
Figure 1. Feedback System

The autonomous $(r_{ref} = 0)$ closed-loop dynamics are given by:

$$\frac{dx_{cl}}{dt} = \mathcal{F}(x_{cl}) \tag{22}$$

where $x_{cl} := [x_6^T, \ x_c]^T \in \mathbb{R}^7$ denotes the closed-loop states and $\mathcal{F}$ is given by Equation (23).

$$\mathcal{F} = \begin{bmatrix} F(x_6) - G(x_6)C_c x_c - G(x_6)D_c M(x_6)^{-1}(H(x_6) - J(x_6)C_c x_c) + G(x_6)u_{3_t} \\ A_c x_c + B_c M(x_6)^{-1} \left(H(x_6) - J(x_6)C_c x_c \right) \end{bmatrix} \tag{23}$$

where $M(x_6) = (I_l + J(x_6) D_c)$. l denotes the number of measurements in y.

The 7-state closed-loop model $\mathcal{F}$, in Equation (23), is nonlinear due to trigonometric terms, $M(x_6)^{-1}$, and polynomial functions to model the aerodynamic coefficients. $\mathcal{F}$ can be approximated by a third degree polynomial function of x_{cl}. The approximation steps are as follows. First, the linearization of $\mathcal{F}$ is computed at $x_{cl} = 0$. Then $\mathcal{F}$ is expressed as $\mathcal{F} := \mathcal{F}_{lin}x_{cl} + \mathcal{F}_{nonl}(x_{cl})$ where $\mathcal{F}_{lin}$ denotes the linearization. Second, each entry of the vector-valued function $\mathcal{F}_{nonl}(x_{cl})$ is approximated by a polynomial consisting of second and third degree terms. The benefit of this procedure is that the polynomial model retains the same linearization as the original nonlinear model.

The polynomial approximation step exploits structure that exists in the nonlinear model. For example, p, q, r, and x_c typically enter linearly with nonlinear functions of α, β, and/or ϕ. To illustrate the point, consider the state-derivative $\dot{\phi} = p + \tan\theta \, (q\sin\phi + r\cos\phi)$ from Equation 12. The value of θ is held at its trim value during approximation. Notice, q and r enters linearly with nonlinear functions of ϕ. By examining each state-derivative separately, insight can be gained on the structure of the nonlinear model.

The assumed structure of the polynomial approximation used in this paper is shown while presenting the approximated closed-loop polynomial model in Appendix B. This structure is used to determine the second and third degree terms to include in the polynomial functions. Then the coefficients of the polynomial functions are computed to approximate Equation (23) over a specified range of the closed-loop state-space. The range of the state space is chosen to be the seven dimensional hypercube in Table 2. The table provides the minimum and maximum deviations of each state from the trim point in Equation (19). Values are

provided in degree for ease of interpretation. The hypercube is uniformly gridded along each dimension by the number of points specified in Table 2. This gridding results in a total of 60000 samples in the hypercube. The nonlinear function $\mathcal{F}_{nonl}$ is evaluated at these points and least squares is used to compute the polynomial coefficients that minimize the difference between $\mathcal{F}_{nonl}$ and the polynomial function at these 60000 samples. The approximation results a cubic degree polynomial model of the form:

$$\dot{x}_{cl} = \mathcal{P}(x_{cl}) \tag{24}$$

$\mathcal{P}$ is provided in Appendix B for both the baseline and the revised controller.

Table 2. State space hypercube data for constructing polynomial models

State	Range: [min max]	Sampled Data Points
β (deg)	$[-10^o \ 10^o]$	5
α (deg)	$[-25^o \ 25^o]$	6
p (deg/s)	$[-35^o \ 35^o/s]$	5
q (deg/s)	$[-30^o/s \ 30^o/s]$	5
r (deg/s)	$[-15^o/s \ 15^o/s]$	5
ϕ (deg)	$[-25^o \ 25^o]$	5
x_c (deg)	$[-20^o \ 20^o]$	4

B.   Polynomial Model Validation

The cubic polynomial models for the baseline and revised control laws involve approximations due to neglecting three aircraft states and due to the polynomial least-squares fits. It is important to determine if the cubic polynomial models are sufficiently accurate. This section compares the polynomial closed-loop models with closed-loop models constructed with the original nine-state nonlinear model (Equation (11)). The term "original model" will refer to the closed loop models constructed with the nine-state nonlinear model. Numerical tools do not exist to rigorously perform this comparison and hence the validation performed in this section relies on heuristic procedures. However, the validation provides some confidence that the polynomial model provides, for engineering purposes, a sufficiently accurate approximation.

The first validation method is to compare the polynomial and original model by simulating from many initial conditions. Numerous simulations have been performed by perturbing the states from their trim values. Most state trajectories are similar for both the polynomial and original model. Figure 2 compares the polynomial and original models with the baseline control law. This specific simulation is performed by perturbing the β, α, p, q, r, ϕ states by 5^0, 20°, 25°, $20^o/s$, $20^o/s$, $5^o/s$, respectively, from their trim points. For the original models, V, θ, and ψ are initialized to their trim values. The simulation results show that the polynomial model is in good agreement with the original model. Note, however, that the α trajectory for the polynomial model diverges from the original model as time progresses. This deviation is large (relative to other states) when the perturbation in the α state is large. However, the simulation comparisons show that the cubic degree polynomial model captures the dynamic characteristics of the original

American Institute of Aeronautics and Astronautics

closed-loop model, even with such large perturbation in the initial condition.

Figure 3 provides a similar comparison of the polynomial and original models with the revised control law. Similar results were obtained at many other simulation initial conditions. This indicates that the polynomial approximation accurately the closed-loop dynamics of the original nonlinear closed-loop model.
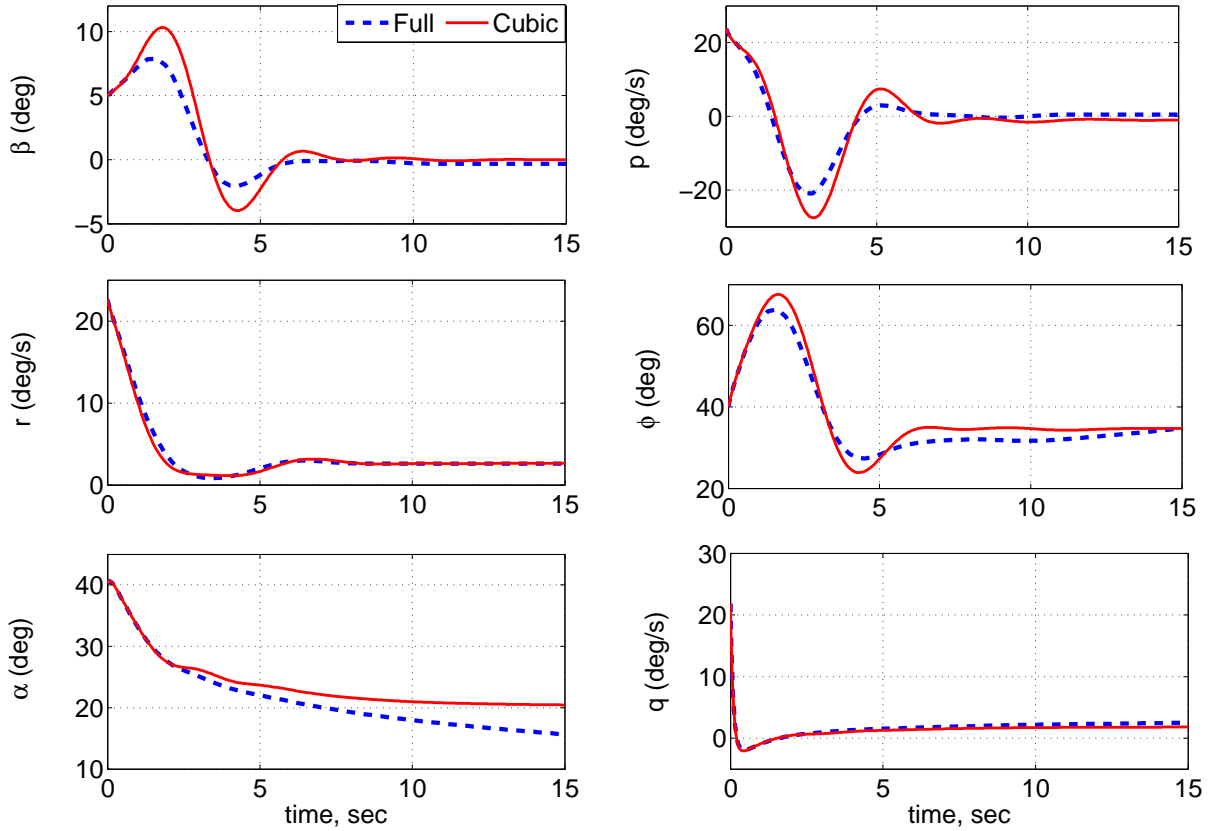

Figure 2. Simulation comparison between the original and approximated closed-loop baseline models due to initial perturbation in the states

The second comparison method provides a statistical quantification on the accuracy of the polynomial model approximation. The closed-loop realization for either of the controllers can be generated by using Equation (23) based on the original nonlinear model. For a given control law, two different seven state realizations are developed: (i) $\mathcal{F}$, based on the original nonlinear model, and (ii) $\mathcal{P}$, a cubic degree polynomial approximation to $\mathcal{P}$. For this comparison, both the models are evaluated by sampling random points within the ellipsoid $x_{cl}{}^T N x_{cl} \leq \bar{\beta}$, where $\bar{\beta}$ is the upper bound of ROA estimation introduced in Section II. The value of $\bar{\beta}$ for both the control law is estimated in Section VI.A. Moreover, the shape matrix N in the ellipsoid is presented in Equation (25). The relative weightings of the diagonal elements of N is determined by the physical operating range of the states around the trim point specified. In other words, the shape matrix roughly scales each state by the maximum magnitude observed during the flight conditions. The maximum magnitude is chosen to be the range of states over which the least squares is performed, as mentioned in Table 2. For ease of interpretation, the shape matrix is also provided in units of degree or degree/sec. However, the computation is performed using the radian representation of N.
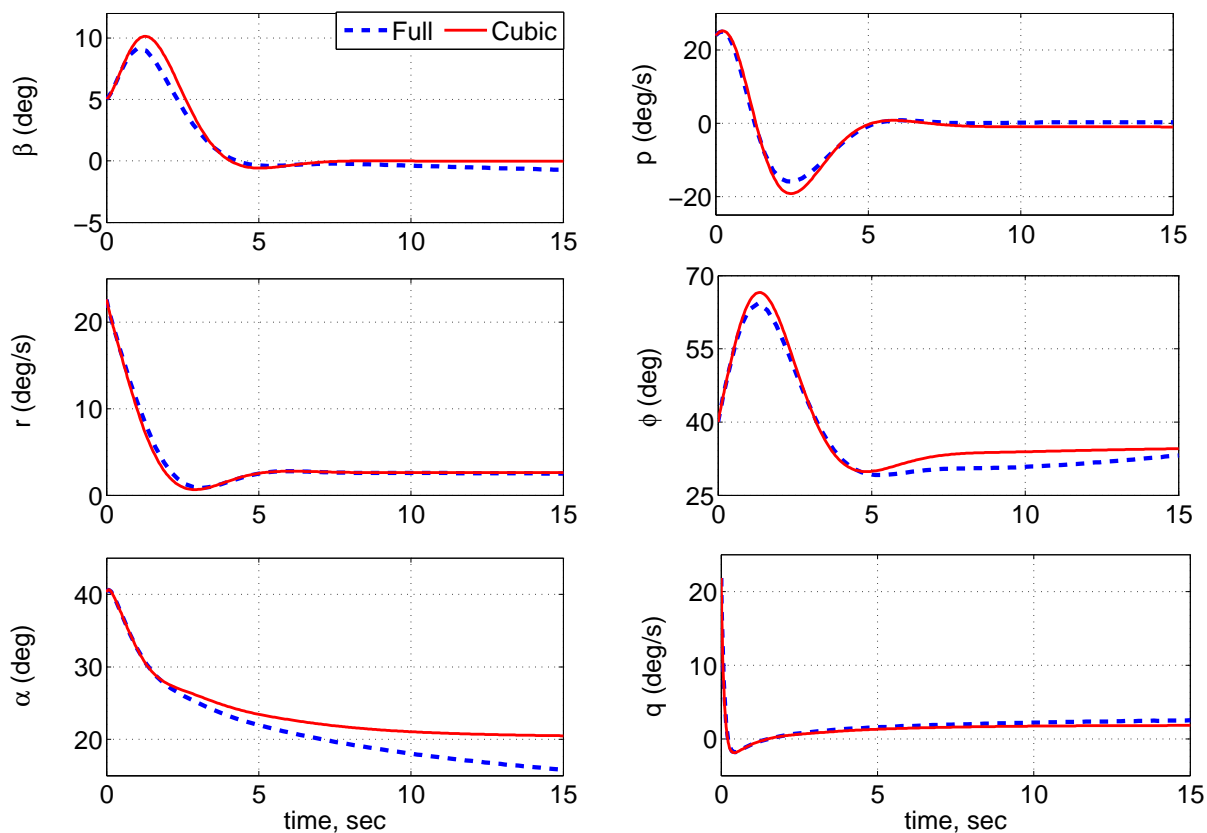
American Institute of Aeronautics and Astronautics

Figure 3. Simulation comparison between the original and approximated closed-loop revised models due to initial perturbation in the states

$$N := diag(0.1745 \text{ rad}, 0.4363 \text{ rad}, 0.6109 \text{ rad/s}, 0.5236 \text{ rad/s}, 0.2618 \text{ rad/s}, 0.4363 \text{ rad}, 0.3491 \text{ rad})^{-2} \quad (25)$$

$$:= diag(10^o, 25^o, 35^o/s, 30^o/s, 15^o/s, 25^o, 20^o)^{-2} \quad (26)$$

Now, define relative error $:= \dfrac{||(\mathcal{F}|_{x_i} - \mathcal{P}|_{x_i})||_2}{||\mathcal{F}|_{x_i}||_2}$, where $x_i \in \mathbb{R}^{7 \times 1}$ satisfies $x_i{}^T N x_i \leq \bar{\beta}$. The relative error, evaluated within the ellipsoid, defines a metric on the notion of how 'close' the approximated model is to the original model. The relative error for the baseline control law is computed at 30,000 different $x_i \in \mathbb{R}^{7 \times 1}$ within the ellipsoid $x_i{}^T N x_i \leq 2.3$. Note, $\bar{\beta} = 2.3$ is taken from Section VI.A. The approximation incurs less than 10% relative error on 88% of the 30,000 points. Similarly, the relative error for the revised control law is also computed at 30,000 different points within the ellipsoid $x_i{}^T N x_i \leq 5.9$. In this case, the approximation incurs less than 10% relative error on approximately 90% of the 30,000 points. Moreover, for both the control laws, the spread of the relative error is uniform as the approximated models deviate away from the trim point.

Both these validation procedure is heuristic since it is still an open problem to develop rigorous and computable metrics of the approximation error between a generic nonlinear (non-analytic) model and a

polynomial model. However, these approaches provide some confidence that the developed polynomial model has captured the dynamic characteristics of the original model, for all engineering purposes.

VI.   Nonlinear Analysis

Extensive linear analyses has been performed to compare the robustness properties of the closed loop systems with the baseline and revised flight control laws.[3] Both the controllers yield similar gain and phase margins, while some of the μ analyses indicated that the revised design has better robustness properties than the baseline. However, linear analysis is only valid within a small region around the operating point which is in general insufficient for analyzing nonlinear phenomenon like the falling leaf motion. This section applies the nonlinear ROA estimation (described in Section II) method to compare the robustness properties of both flight control laws. The analyses are performed for the operating point mentioned in Equation (19) using the cubic polynomial closed-loop models developed in Section V.

A.   Estimation of Upper Bound on ROA

The Monte Carlo search, described in Section II, is used to estimate ROA upper bounds $\bar{\beta}$ for both flight control laws. The Monte Carlo search was performed with 2 million simulations each for the baseline and revised control laws. The search returns an initial condition x_0 on the boundary of the ellipsoid, i.e. $p(x_0) = x_0^T N x_0 = \bar{\beta}_{MC}$, that causes the system to go unstable. Hence, the value of the $\bar{\beta}_{MC}$ provides an upper bound of the ROA for the F/A-18 aircraft. Recall that the shape matrix N is defined in Equation (25). The baseline control law provides an upper bound of $\bar{\beta}_{MC} = 2.298$ whereas the revised control law provides an upper bound of $\bar{\beta}_{MC} = 5.836$.

The Monte Carlo search returned the following initial condition for the closed system with the baseline control law:

$$x_0 = [-5.632^o,\ -33.54^o/s,\ 7.908^o/s,\ 0.6103^o,\ 3.959^o,\ 6.107^o/s,\ 0.06820^o]^T$$

This initial condition satisfies $p(x_0) = 2.298$. Figure 4 shows the unstable response of the baseline system resulting from this initial condition. Decreasing the initial condition slightly to $0.995x_0$ leads to a stable response.

For the revised control law the Monte Carlo search returned the following initial condition:

$$x_0 = [3.841^o,\ 54.25^o/s,\ 8.705^o/s,\ 29.45^o,\ 1.641^o,\ 0.630^o/s,\ 0.7880^o]^T$$

This initial condition satisfies $p(x_0) = 5.895$ and Figure 5 shows the unstable response of the revised system resulting from this initial condition. Again, a stable initial condition is obtained by slightly decreasing the initial condition to $0.995x_0$.
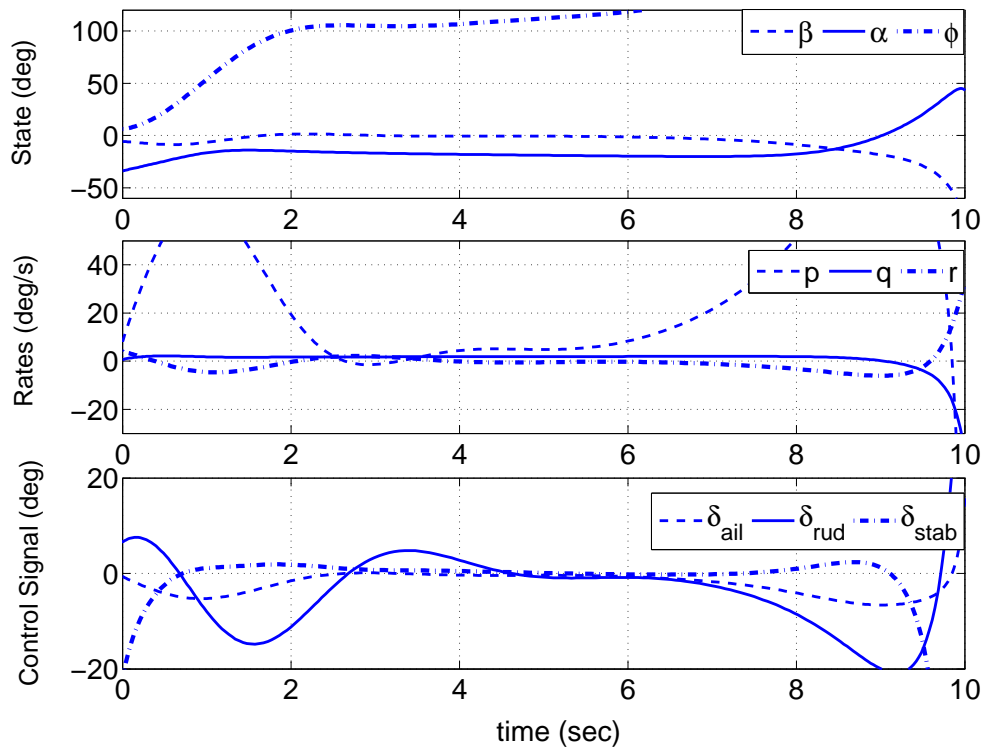
American Institute of Aeronautics and Astronautics

Figure 4. Unstable trajectories for Baseline control law with IC s.t. $x_o^T N x_o = 2.298$
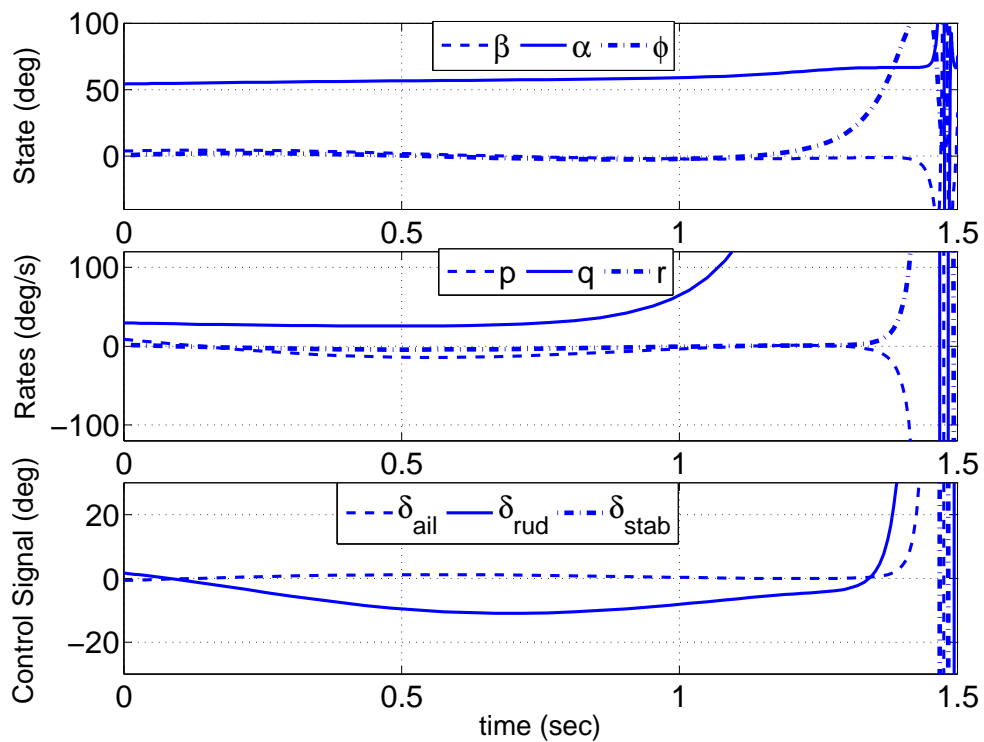

Figure 5. Unstable trajectories for Revised control law with IC s.t. $x_o^T N x_o = 5.895$

B. Estimation of Lower Bound on ROA

The V-s iteration, described in Section II, is employed to estimate the ROA lower bounds $\underline{\beta}$ for both the F/A-18 flight control laws. Recall, $N = N^T$ indicates the shape matrix of ellipsoid and is determined by the physical operating range of the states around the trim point specified. N is provided by Equation (25). The ellipsoid, $x_{cl}^T N x_{cl} = \underline{\beta}$, defines the set of initial conditions for which the control law will bring the aircraft back to its trim point. The state corresponding to the smaller diagonal element of N is expected to have a wide range of variation in estimating the region of attraction. If the aircraft is perturbed due to a wind gust or other upset condition but remains in the ellipsoid then the control law will recover the vehicle back to trim. In other words the ellipsoid defines a safe flight envelope for the F/A-18. Hence, the ROA provides a measure of how much perturbation the aircraft can tolerate before it becomes unstable. Roughly, the value of the $\underline{\beta}$ can be thought of as 'nonlinear stability margin', similar to the linear stability margin (k_m) concept presented in the linear analysis.[3] However, these two margins are not directly comparable to each other.

Increasing the degree of the Lyapunov function improves the lower bound estimate of the ROA as discussed in Section II. At first, bounds using the quadratic Lyapunov function from linearized analysis, denoted as $\underline{\beta}_{LIN}$, are computed. This method has been proposed for validation of flight control laws.[1] The baseline flight control law achieves a bound of $\underline{\beta}_{LIN} = 5.100 \times 10^{-3}$ while the revised achieves $\underline{\beta}_{LIN} = 8.200 \times 10^{-3}$. Recall, the upper bound estimation, $\bar{\beta}_{MC}$, of the ROA is 2.298 for baseline and 5.895 for the revised flight control law. These lower bounds are not particularly useful since they are three orders of magnitude smaller than the corresponding upper bounds. The estimate of the lower bound needs to be improved. Hence, the V-s iteration with quadratic and quartic Lyapunov functions are used to increase the lower bound estimate.

The V-s iteration with quadratic Lyapunov functions gives $\underline{\beta}_2 = 0.8921$ for the baseline control law and $\underline{\beta}_2 = 3.719$ for the revised control law. The lower bound estimation was improved dramatically compared to the linearized Lyapunov analysis. However, the estimation can be further improved by using quartic Lyapunov function. The V-s iteration with quartic Lyapunov functions is $\underline{\beta}_4 = 2.006$ for the baseline control law and $\underline{\beta}_4 = 4.299$ for the revised control law. These bounds are significantly larger than the bounds obtained for the linearized Lyapunov function. A sixth order Lyapunov function can lead to improved lower bounds but with a significant increase in computation time. The lower bounds with different degree of Lyapunov function show that the linearized ROA method is much more conservative than the results obtained using the quartic Lyapunov function.

C. Discussion

The largest ellipsoid contained in the region of attraction is denoted as $\mathcal{E}_{\beta^*} := \{x_{cl} \in \mathbb{R}^7 \ : \ x_{cl}^T N x_{cl} \leq \beta^*\}$. The lower and upper bounds on β^* have been computed for the closed-loop systems with both F/A-18 flight control laws. The bounds on β^* for the baseline control law are: $2.006 \leq \beta^* \leq 2.298$. For the revised control law the bounds are: $4.299 \leq x_{cl}^T N x_{cl} \leq 5.895$. These bounds on the ROA can be visualized by plotting slices of the ellipsoid $x_{cl}^T N x_{cl}$. Figure 6 and 7 show slices of both the inner/outer approximations of the best ellipsoidal ROA approximation for both the flight control laws, respectively in α-β and p-r planes. These

states are chosen since they play an important role in characterizing the falling leaf motion. In both the figures, the solid lines show the slices of the inner bounds obtained from quartic Lyapunov analysis. Every initial condition within the solid ellipses will return to the trim condition (marked as a '+'). If the aircraft is perturbed due to an upset condition or wind gust but remains within this ellipsoid then the control law will recover the aircraft and bring it back to trim. The dashed lines show the slices of the outer bounds obtained from Monte Carlo analysis. There is at least one initial condition on the outer ellipsoid which leads to a divergent trajectory. The ellipsoid is seven dimensional and hence the initial condition leading to a divergent trajectory does not necessarily lie on the slice of the ellipsoid shown in the figure. Upset conditions that push the aircraft state to this upper bound ellipsoid could potentially lead to loss of control.
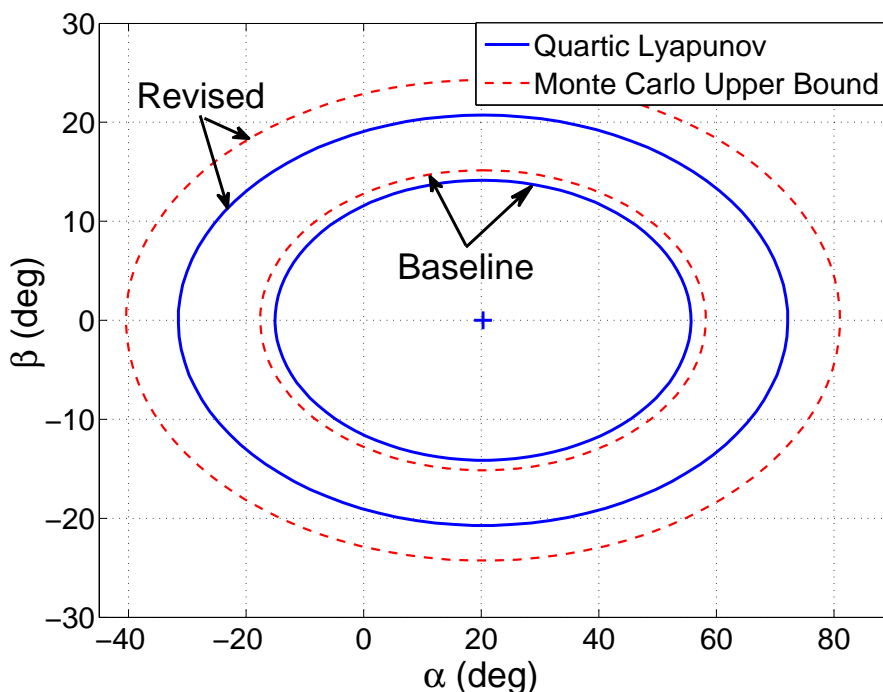
Figure 6. Lower / upper bound slices for ROA estimate in $\alpha - \beta$ plane. The lower bound estimate is based on the quartic Lyapunov function.

The closeness of these upper/lower bounds indicate that the best ellipsoidal ROA approximation problem has been solved for engineering purposes. Hence, definitive conclusions regarding the stability region about the flight control laws can be drawn for the F/A-18 aircraft. The slices for the quartic Lyapunov functions demonstrate that the ROA estimate for the revised control law is larger than the one for the baseline control law. For example, from the α-β slice it can be concluded that the baseline controller returns to the trim condition for initial perturbations in an ellipse defined by β between (approximately) -14° and $+14^o$ and α between (approximately) -15 and $+55^o$. The revised controller returns to the trim condition for initial perturbations in an ellipse defined by β between -21° and $+21^o$ and α between -32° and $+72^o$. It is important to note that, the revised controller is better able to damp out the sideslip motion and consequently, increasing the dutch-roll damping. It has been shown that increased dutch-roll damping due to the revised
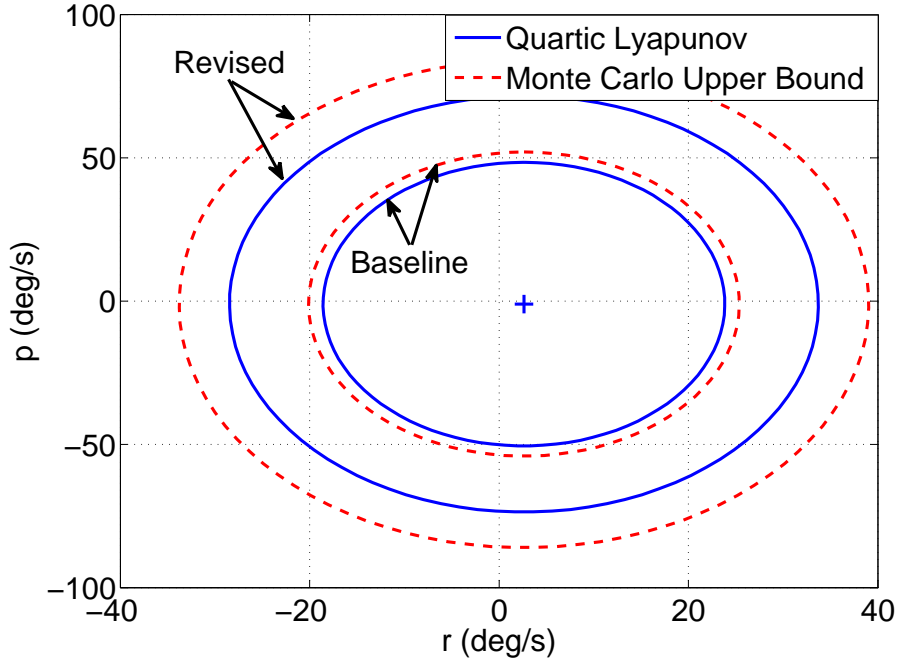
American Institute of Aeronautics and Astronautics

Figure 7. Lower / upper bound slices for ROA estimate in $p - r$. The lower bound estimate is based on the quartic Lyapunov function.

flight control law architecture is one of the key reasons to suppress the falling leaf motion.[2] Figure 6 shows that the sideslip damping has significantly improved in the revised flight control law compared to the baseline design. The stability region also increases along other state direction under the revised flight control law. Moreover, the aircraft also achieves an increased stability region along the angle-of-attack direction with the revised design. Overall, the suppression of the falling leaf can be attributed to the larger stability region provided by the revised flight control law.

In fact, the robustness improvement for the revised controller is more dramatic if the volume of the ROA estimate is considered. The volume of the ellipsoid $\mathcal{E}_\beta$ is proportional to $\beta^{(n/2)}$ where $n = 7$ is the state dimension. Thus the ROA estimate obtained by the revised control law has a volume which is $(\underline{\beta}_{4,rev}/\underline{\beta}_{4,base})^{3.5}$ greater than that obtained by the baseline design. This corresponds to a volume increase of 14.3 for the revised flight control law. Thus information from these two ellipsoids can be used to draw conclusions about the safe flight envelope. The size of these ellipsoids measure the robustness of the flight control law to disturbances. In summary, the ellipsoids define a metric for the safe flight envelope of the F/A-18 aircraft. Based on this metric, the revised control law has an increased safe flight envelope, which helps suppressing the falling leaf motion.

The nonlinear analysis imposes a limitation that the dynamics of the aircraft need to be described by the polynomial functions of the states. Hence, the caveat with this nonlinear analysis results is that the size of the ROA may be larger than where the polynomial model is valid. Due to the approximation procedure, the approximated polynomial model deviates from the original model away from the trim points.

American Institute of Aeronautics and Astronautics

As a cross-validation, both the approximated and the original model are simulated by sampling the initial conditions on the ellipsoid $x_{cl}^T N x_{cl} = \bar{\beta}$. Numerous simulation comparisons revealed that both the models' state trajectories are in good agreement, in light of the discussion of Section V.B. Moreover, the heuristic statistical method of model validation, performed in Section V.B, also provides some confidence on the validity of the approximated model on the boundary of the outer ellipsoidal approximation.

The computation time required for the lower bounds is summarized in Table 3. The quartic Lyapunov functions provided much better lower bounds than the quadratic Lyapunov functions. However, computing bounds with quartic Lyapunov functions required significantly more time than computing bounds with quadratic Lyapunov functions. This is due to the computational growth of SOS optimizations due to an increase in the degree of the polynomial model. Increasing the state dimension, e.g. by including the V and θ states, also would result in a large increase in computation for the lower bounds. The analyses are performed on Intel(R) Core(TM) i7 CPU 2.67GHz 8.00GB RAM.

Table 3. Computational time for estimating lower bound of ROA with V-s iteration procedure

Plant	Lyapunov Degree	Iteration Steps	Baseline	Revised
7-State, Cubic Degree	4th	80	7.935 Hrs	7.365 Hrs
	2nd	40	0.113 Hrs	0.111 Hrs
7-State Linear	2nd	40	0.00340 Hrs	0.00440 Hrs

VII.   Summary

This paper estimated bounds on the regions of attraction for two F/A flight control laws. Upper bounds were estimated using Monte Carlo simulations and lower bounds were estimated using sum of squares optimization. It is important to note that the ROA analysis accounts for significant nonlinearities in the F/A-18 aircraft dynamics. This makes the analysis more applicable to nonlinear flight phenomenon such as the falling leaf mode. The conclusion of this analysis is that the revised F/A-18 flight control law has a significantly larger region of attraction than the baseline control law. This nonlinear analysis indicates that revised control law is less susceptible to to a loss of control phenomenon like the falling leaf mode.

VIII.   Acknowledgments

American Institute of Aeronautics and Astronautics

Appendix

A. Aerodynamic Coefficients

The aerodynamic coefficients presented here have been extracted from various papers.[26–30,35] The aerodynamic model of the aircraft is presented here as closed-form expression. Moreover, the MATLAB M-files to generate the models and the results shown in this paper can also be found in the website: *http://www.aem.umn.edu/ AerospaceControl/*

$$
\text{Pitching Moment,} \ \ C_m = (C_{m_{\alpha_2}}\alpha^2 + C_{m_{\alpha_1}}\alpha + C_{m_{\alpha_0}}) + (C_{m_{\delta_{stab_2}}}\alpha^2 + C_{m_{\delta_{stab_1}}}\alpha + C_{m_{\delta_{stab_0}}})\delta_{stab}
$$
$$
+ \frac{\bar{c}}{2V_T}(C_{m_{q_3}}\alpha^3 + C_{m_{q_2}}\alpha^2 + C_{m_{q_1}}\alpha + C_{m_{q_0}})q
$$

$$
\text{Rolling Moment,} \ \ C_l = (C_{l_{\beta_4}}\alpha^4 + C_{l_{\beta_3}}\alpha^3 + C_{l_{\beta_2}}\alpha^2 + C_{l_{\beta_1}}\alpha + C_{l_{\beta_0}})\beta
$$
$$
+ (C_{l_{\delta_{ail_3}}}\alpha^3 + C_{l_{\delta_{ail_2}}}\alpha^2 + C_{l_{\delta_{ail_1}}}\alpha + C_{l_{\delta_{ail_0}}})\delta_{ail}
$$
$$
+ (C_{l_{\delta_{rud_3}}}\alpha^3 + C_{l_{\delta_{rud_2}}}\alpha^2 + C_{l_{\delta_{rud_1}}}\alpha + C_{l_{\delta_{rud_0}}})\delta_{rud}
$$
$$
+ \frac{b}{2V_T}(C_{l_{p_1}}\alpha + C_{l_{p_0}})p + \frac{b}{2V_T}(C_{l_{r_2}}\alpha^2 + C_{l_{r_1}}\alpha + C_{l_{r_0}})r
$$

$$
\text{Yawing Moment,} \ \ C_n = (C_{n_{\beta_2}}\alpha^2 + C_{n_{\beta_1}}\alpha + C_{n_{\beta_0}})\beta
$$
$$
+ (C_{n_{\delta_{rud_4}}}\alpha^4 + C_{n_{\delta_{rud_3}}}\alpha^3 + C_{n_{\delta_{rud_2}}}\alpha^2 + C_{n_{\delta_{rud_1}}}\alpha + C_{n_{\delta_{rud_0}}})\delta_{rud}
$$
$$
+ (C_{n_{\delta_{ail_3}}}\alpha^3 + C_{n_{\delta_{ail_2}}}\alpha^2 + C_{n_{\delta_{ail_1}}}\alpha + C_{n_{\delta_{ail_0}}})\delta_{ail}
$$
$$
+ \frac{b}{2V_T}(C_{n_{p_1}}\alpha + C_{n_{p_0}})p + \frac{b}{2V_T}(C_{n_{r_1}}\alpha + C_{n_{r_0}})r
$$

$$
\text{Sideforce Coefficient,} \ \ C_Y = (C_{Y_{\beta_2}}\alpha^2 + C_{Y_{\beta_2}}\alpha + C_{Y_{\beta_0}})\beta
$$
$$
+ (C_{Y_{\delta_{ail_3}}}\alpha^3 + C_{Y_{\delta_{ail_2}}}\alpha^2 + C_{Y_{\delta_{ail_1}}}\alpha + C_{Y_{\delta_{ail_0}}})\delta_{ail}
$$
$$
+ (C_{Y_{\delta_{rud_3}}}\alpha^3 + C_{Y_{\delta_{rud_2}}}\alpha^2 + C_{Y_{\delta_{rud_1}}}\alpha + C_{Y_{\delta_{rud_0}}})\delta_{rud}
$$

$$
\text{Lift Coefficient,} \ \ C_L = (C_{L_{\alpha_3}}\alpha^3 + C_{L_{\alpha_2}}\alpha^2 + C_{L_{\alpha_1}}\alpha + C_{L_{\alpha_0}})\cos(\frac{2\beta}{3})
$$
$$
+ (C_{L_{\delta_{stab_3}}}\alpha^3 + C_{L_{\delta_{stab_2}}}\alpha^2 + C_{L_{\delta_{stab_1}}}\alpha + C_{L_{\delta_{stab_0}}})\delta_{stab}
$$

$$
\text{Drag Coefficient,} \ \ C_D = (C_{D_{\alpha_4}}\alpha^4 + C_{D_{\alpha_3}}\alpha^3 + C_{D_{\alpha_2}}\alpha^2 + C_{D_{\alpha_1}}\alpha + C_{D_{\alpha_0}})\cos\beta + C_{D_0}
$$
$$
+ (C_{D_{\delta_{stab_3}}}\alpha^3 + C_{D_{\delta_{stab_2}}}\alpha^2 + C_{D_{\delta_{stab_1}}}\alpha + C_{D_{\delta_{stab_0}}})\delta_{stab}
$$

Table 4. Aerodynamic Moment Coefficients

Pitching Moment			Rolling Moment			Yawing Moment		
$C_{m_{\alpha_2}}$	=	-1.2897	$C_{l_{\beta_4}}$	=	-1.6196	$C_{n_{\beta_2}}$	=	-0.3816
$C_{m_{\alpha_1}}$	=	0.5110	$C_{l_{\beta_3}}$	=	2.3843	$C_{n_{\beta_1}}$	=	0.0329
$C_{m_{\alpha_0}}$	=	-0.0866	$C_{l_{\beta_2}}$	=	-0.3620	$C_{n_{\beta_0}}$	=	0.0885
$C_{m_{\delta_{stab_2}}}$	=	0.9338	$C_{l_{\beta_1}}$	=	-0.4153	$C_{n_{\delta_{ail_3}}}$	=	0.2694
$C_{m_{\delta_{stab_1}}}$	=	-0.3245	$C_{l_{\beta_0}}$	=	-0.0556	$C_{n_{\delta_{ail_2}}}$	=	-0.3413
$C_{m_{\delta_{stab_0}}}$	=	-0.9051	$C_{l_{\delta_{ail_3}}}$	=	0.1989	$C_{n_{\delta_{ail_1}}}$	=	0.0584
$C_{m_{q_3}}$	=	64.7190	$C_{l_{\delta_{ail_2}}}$	=	-0.2646	$C_{n_{\delta_{ail_0}}}$	=	0.0104
$C_{m_{q_2}}$	=	-68.5641	$C_{l_{\delta_{ail_1}}}$	=	-0.0516	$C_{n_{\delta_{rud_4}}}$	=	0.3899
$C_{m_{q_1}}$	=	10.9921	$C_{l_{\delta_{ail_0}}}$	=	0.1424	$C_{n_{\delta_{rud_3}}}$	=	-0.8980
$C_{m_{q_0}}$	=	-4.1186	$C_{l_{\delta_{rud_3}}}$	=	-0.0274	$C_{n_{\delta_{rud_2}}}$	=	0.5564
			$C_{l_{\delta_{rud_2}}}$	=	0.0083	$C_{n_{\delta_{rud_1}}}$	=	-0.0176
			$C_{l_{\delta_{rud_1}}}$	=	0.0014	$C_{n_{\delta_{rud_0}}}$	=	-0.0780
			$C_{l_{\delta_{rud_0}}}$	=	0.0129	$C_{n_{p_1}}$	=	-0.0881
			$C_{l_{p_1}}$	=	0.2377	$C_{n_{p_0}}$	=	0.0792
			$C_{l_{p_0}}$	=	-0.3540	$C_{n_{r_1}}$	=	-0.1307
			$C_{l_{r_2}}$	=	-1.0871	$C_{n_{r_0}}$	=	-0.4326
			$C_{l_{r_1}}$	=	0.7804			
			$C_{l_{r_0}}$	=	0.1983			

Table 5. Aerodynamic Force Coefficients

Sideforce Coefficient			Drag Force Coefficient			Lift Force Coefficient		
$C_{Y_{\beta_2}}$	=	-0.1926	$C_{D_{\alpha_4}}$	=	1.4610	$C_{L_{\alpha_3}}$	=	1.1645
$C_{Y_{\beta_1}}$	=	0.2654	$C_{D_{\alpha_3}}$	=	-5.7341	$C_{L_{\alpha_2}}$	=	-5.4246
$C_{Y_{\beta_0}}$	=	-0.7344	$C_{D_{\alpha_2}}$	=	6.3971	$C_{L_{\alpha_1}}$	=	5.6770
$C_{Y_{\delta_{ail_3}}}$	=	-0.8500	$C_{D_{\alpha_1}}$	=	-0.1995	$C_{L_{\alpha_0}}$	=	-0.0204
$C_{Y_{\delta_{ail_2}}}$	=	1.5317	$C_{D_{\alpha_0}}$	=	-1.4994	$C_{L_{\delta_{stab_3}}}$	=	2.1852
$C_{Y_{\delta_{ail_1}}}$	=	-0.2403	C_{D_0}	=	1.5036	$C_{L_{\delta_{stab_2}}}$	=	-2.6975
$C_{Y_{\delta_{ail_0}}}$	=	-0.1656	$C_{D_{\delta_{stab_3}}}$	=	-3.8578	$C_{L_{\delta_{stab_1}}}$	=	0.4055
$C_{Y_{\delta_{rud_3}}}$	=	0.9351	$C_{D_{\delta_{stab_2}}}$	=	4.2360	$C_{L_{\delta_{stab_0}}}$	=	0.5725
$C_{Y_{\delta_{rud_2}}}$	=	-1.6921	$C_{D_{\delta_{stab_1}}}$	=	-0.2739			
$C_{Y_{\delta_{rud_1}}}$	=	0.4082	$C_{D_{\delta_{stab_0}}}$	=	0.0366			
$C_{Y_{\delta_{rud_0}}}$	=	0.2054						

B.   Closed-loop Polynomial Model

The closed-loop cubic degree polynomial models discussed in Section V are presented below. Moreover, the MATLAB M-files to generate the models can also be found in the website:

http://www.aem.umn.edu/ AerospaceControl/

Baseline Polynomial Model

The cubic degree polynomial approximation for the closed-loop system with the baseline control law is:

$$\dot{\beta} = -3.978 \times 10^{-3}\alpha^3 - 2.191 \times 10^{-1}\alpha^2\beta + 2.9427 \times 10^{-5}\alpha^2\phi - 2.458 \times 10^{-3}\alpha\beta^2$$
$$+ 5.509 \times 10^{-2}\alpha\beta\phi - 4.330 \times 10^{-5}\alpha\phi^2 + 6.2222 \times 10^{-2}\beta^3 - 1.672 \times 10^{-2}\beta^2\phi$$
$$+ 2.785 \times 10^{-3}\beta\phi^2 - 6.786 \times 10^{-3}\phi^3 + 2.708 \times 10^{-2}\alpha^2 + 2.017 \times 10^{-1}\alpha\beta$$
$$- 5.323 \times 10^{-5}\alpha\phi - 2.698 \times 10^{-2}\beta^2 + 2.729 \times 10^{-2}\beta\phi - 2.747 \times 10^{-2}\phi^2$$
$$+ (-3.181 \times 10^{-1}\alpha^2 + 3.466 \times 10^{-2}\beta^2 + 9.638 \times 10^{-1}\alpha)p$$
$$+ (-3.634 \times 10^{-1}\alpha\beta + 2.708 \times 10^{-1}\beta)q$$
$$+ (4.009 \times 10^{-1}\alpha^2 - 5.344 \times 10^{-3}\beta^2 + 3.141 \times 10^{-1}\alpha)r$$
$$+ (2.496 \times 10^{-2}\alpha^2 - 2.630 \times 10^{-2}\beta^2 - 5.127 \times 10^{-2}\alpha)x_{c_B}$$
$$+ -1.411 \times 10^{-3}\alpha + 2.314 \times 10^{-2}\beta + 3.474 \times 10^{-1}p + 7.134 \times 10^{-2}\phi$$
$$- 9.225 \times 10^{-1}r + 1.406 \times 10^{-2}x_{c_B}$$

$$\dot{\alpha} = -2.139 \times 10^{-1}\alpha^3 + 7.550 \times 10^{-3}\alpha^2\beta + 3.540 \times 10^{-2}\alpha^2\phi - 1.846 \times 10^{-2}\alpha\beta^2$$
$$- 4.181 \times 10^{-5}\alpha\beta\phi + 1.029 \times 10^{-2}\alpha\phi^2 - 4.365 \times 10^{-3}\beta^3 - 4.154 \times 10^{-3}\beta^2\phi$$
$$- 6.8825 \times 10^{-5}\beta\phi^2 + 1.252 \times 10^{-2}\phi^3 + 3.637 \times 10^{-1}\alpha^2 - 5.181 \times 10^{-2}\alpha\beta$$
$$+ 1.364 \times 10^{-2}\alpha\phi - 2.243 \times 10^{-2}\beta^2 + 1.093 \times 10^{-4}\beta\phi - 3.648 \times 10^{-2}\phi^2$$
$$+ (6.357 \times 10^{-1}\alpha\beta - 9.576 \times 10^{-1}\beta)p$$
$$+ (-1.132\alpha^2 + 1.988 \times 10^{-1}\beta^2 + 6.941 \times 10^{-1}\alpha)q$$
$$+ (-7.499 \times 10^{-1}\alpha\beta - 3.619 \times 10^{-1}\beta)r$$
$$+ -2.299 \times 10^{-1}\alpha + 1.870 \times 10^{-3}\beta - 4.688 \times 10^{-2}\phi + 7.259 \times 10^{-1}q$$

$$\dot{p} = -3.314 \times 10^{-2}\alpha^3 - 19.69\alpha^2\beta - 1.646 \times 10^{-3}\alpha\beta^2 + 18.79\beta^3 - 8.022 \times 10^{-2}\alpha^2$$
$$+ 15.86\alpha\beta + 1.219 \times 10^{-3}\beta^2 + (-5.204 \times 10^{-1}\alpha^2 + 1.252\alpha)p$$
$$+ (-4.737\alpha^2 + 6.823 \times 10^{-2}\alpha)r - 8.150 \times 10^{-1}qr - 3.173 \times 10^{-2}pq$$
$$+ (-2.056\alpha^2 + 3.553 \times 10^{-2}\alpha)x_{c_B} + 4.916 \times 10^{-2}\alpha - 7.366\beta - 9.538 \times 10^{-1}p$$
$$- 3.688 \times 10^{-2}q + 1.479r + 6.513 \times 10^{-1}x_{c_B}$$

$$\dot{q} = 1.553\alpha^3 - 2.174\alpha^2 + (17.13\alpha^2 + 4.40\alpha)q - 1.964 \times 10^{-2}r^2 + 9.712 \times 10^{-1}pr$$
$$+ 1.964 \times 10^{-2}p^2 + (-2.303\alpha + 4.393 \times 10^{-2}p - 14.56q - 2.026 \times 10^{-2}r)$$

American Institute of Aeronautics and Astronautics

$$\dot{r} = -3.196 \times 10^{-2}\alpha^3 - 1.678\alpha^2\beta + 1.274 \times 10^{-2}\alpha\beta^2 - 3.236 \times 10^{-1}\beta^3$$
$$+ 3.869 \times 10^{-2}\alpha^2 - 1.795\alpha\beta - 9.442 \times 10^{-3}\beta^2$$
$$+ (-9.543 \times 10^{-2}\alpha^2 + 2.081 \times 10^{-2}\alpha)p + (-5.179 \times 10^{-1}\alpha^2 + 4.541 \times 10^{-1}\alpha)r$$
$$+ 3.173 \times 10^{-2}qr - 7.543 \times 10^{-1}pq + (-5.102 \times 10^{-1}\alpha^2 + 4.497 \times 10^{-1}\alpha)x_{c_B}$$
$$+ -1.329 \times 10^{-2}\alpha + 5.164 \times 10^{-1}\beta + 5.438 \times 10^{-3}p + 1.579 \times 10^{-2}q$$
$$- 5.042 \times 10^{-1}r - 3.129 \times 10^{-1}x_{c_B}$$

$$\dot{\phi} = (-1.481 \times 10^{-1}\phi^2 + 2.921 \times 10^{-1}\phi)q + (-7.226 \times 10^{-2}\phi^2 - 2.181 \times 10^{-1}\phi)r$$
$$+ p + 1.941 \times 10^{-1}q + 2.772 \times 10^{-1}r$$

$$\dot{x}_{c_B} = 4.900r - x_{c_B}$$

Revised Polynomial Model

The cubic degree polynomial approximation for the closed-loop system with the revised control law is:

$$\dot{\beta} = 3.153 \times 10^{-6}\alpha^3 - 2.065 \times 10^{-1}\alpha^2\beta + 1.958 \times 10^{-3}\alpha^2\phi - 1.360 \times 10^{-3}\alpha\beta^2$$
$$+ 5.556 \times 10^{-2}\alpha\beta\phi - 4.814 \times 10^{-4}\alpha\phi^2 + 5.772 \times 10^{-2}\beta^3 - 1.964 \times 10^{-2}\beta^2\phi$$
$$+ 3.563 \times 10^{-3}\beta\phi^2 - 6.644 \times 10^{-3}\phi^3 + 2.404 \times 10^{-2}\alpha^2 + 1.717 \times 10^{-1}\alpha\beta$$
$$- 6.328 \times 10^{-3}\alpha\phi - 2.454 \times 10^{-2}\beta^2 + 2.606 \times 10^{-2}\beta\phi - 2.771 \times 10^{-2}\phi^2$$
$$+ (-3.010 \times 10^{-1}\alpha^2 + 2.034 \times 10^{-2}\beta^2 + 9.247 \times 10^{-1}\alpha)p$$
$$+ (-3.634 \times 10^{-1}\alpha\beta + 2.708 \times 10^{-1}\beta)q$$
$$+ (3.558 \times 10^{-1}\alpha^2 + 3.255 \times 10^{-2}\beta^2 + 4.181 \times 10^{-1}\alpha)r$$
$$+ (2.576 \times 10^{-2}\alpha^2 - 2.700 \times 10^{-2}\beta^2 - 5.287 \times 10^{-2}\alpha)x_{c_R}$$
$$+ -1.434 \times 10^{-3}\alpha + 2.750 \times 10^{-2}\beta + 3.529 \times 10^{-1}p$$
$$+ 7.253 \times 10^{-2}\phi - 9.372 \times 10^{-1}r + 1.429 \times 10^{-2}x_{c_R}$$

$$\dot{\alpha} = -2.139 \times 10^{-1}\alpha^3 + 7.550 \times 10^{-3}\alpha^2\beta + 3.540 \times 10^{-2}\alpha^2\phi - 1.845 \times 10^{-2}\alpha\beta^2$$
$$- 4.182 \times 10^{-5}\alpha\beta\phi + 1.029 \times 10^{-2}\alpha\phi^2 - 4.365 \times 10^{-3}\beta^3 - 4.154 \times 10^{-3}\beta^2\phi$$
$$- 6.883 \times 10^{-5}\beta\phi^2 + 1.252 \times 10^{-2}\phi^3 + 3.637 \times 10^{-1}\alpha^2 - 5.181 \times 10^{-2}\alpha\beta$$
$$+ 1.364 \times 10^{-2}\alpha\phi - 2.243 \times 10^{-2}\beta^2 + 1.093 \times 10^{-4}\beta\phi - 3.649 \times 10^{-2}\phi^2$$
$$+ (6.357 \times 10^{-1}\alpha\beta - 9.576 \times 10^{-1}\beta)p$$
$$+ (-1.132\alpha^2 + 1.988 \times 10^{-1}\beta^2 + 6.941 \times 10^{-1}\alpha)q$$
$$+ (-7.499 \times 10^{-1}\alpha\beta - 3.619 \times 10^{-1}\beta)r$$
$$+ -2.299 \times 10^{-1}\alpha + 1.871 \times 10^{-3}\beta - 4.688 \times 10^{-2}\phi + 7.259 \times 10^{-1}q$$

$$\dot{p} = -4.415 \times 10^{-1}\alpha^3 - 23.22\alpha^2\beta - 7.476 \times 10^{-1}\alpha^2\phi - 2.556 \times 10^{-1}\alpha\beta^2$$
$$+ 20.20\beta^3 + 2.031 \times 10^{-1}\alpha^2 + 20.65\alpha\beta + 1.149\alpha\phi + 6.667 \times 10^{-2}\beta^2$$
$$+ (-5.104\alpha^2 + 7.496\alpha)p + (7.453\alpha^2 - 16.52\alpha)r$$
$$- 3.173 \times 10^{-2}pq - 8.151 \times 10^{-1}qr + (-2.227\alpha^2 + 2.823 \times 10^{-1}\alpha)x_{c_R}$$
$$+ 6.123 \times 10^{-2}\alpha - 9.701\beta - 3.923p - 6.103 \times 10^{-1}\phi$$
$$- 3.688 \times 10^{-2}q + 9.365r + 5.311 \times 10^{-1}x_{c_R}$$

$$\dot{q} = 1.554\alpha^3 - 2.175\alpha^2 + (17.13\alpha^2 + 4.404\alpha)q + 1.964 \times 10^{-2}p^2 - 1.964 \times 10^{-2}r^2$$
$$+ 9.713 \times 10^{-1}pr + -2.303\alpha + 4.393 \times 10^{-2}p - 14.55q - 2.026 \times 10^{-2}r$$

$$\dot{r} = -2.469 \times 10^{-1}\alpha^3 - 2.324\alpha^2\beta + 9.538 \times 10^{-2}\alpha\beta^2 - 4.018 \times 10^{-2}\beta^3$$
$$+ 1.781 \times 10^{-1}\alpha^2 - 1.419\alpha\beta - 2.519 \times 10^{-2}\beta^2$$
$$+ (-9.357 \times 10^{-1}\alpha^2 + 5.264 \times 10^{-1}\alpha)p + (1.7156\alpha^2 - 8.8988 \times 10^{-1}\alpha)r$$
$$+ 3.173 \times 10^{-2}qr - 7.544 \times 10^{-1}pq + (-5.427 \times 10^{-1}\alpha^2 + 4.694 \times 10^{-1}\alpha)x_{c_R}$$
$$+ (-1.344 \times 10^{-2}\alpha + 5.455 \times 10^{-1}\beta + 4.254 \times 10^{-2}p + 7.624 \times 10^{-3}\phi$$
$$+ 1.579 \times 10^{-2}q - 6.027 \times 10^{-1}r - 3.114 \times 10^{-1}x_{c_R})$$

$$\dot{\phi} = (-1.481 \times 10^{-1}\phi^2 + 2.921 \times 10^{-1}\phi)q + (-7.226 \times 10^{-2}\phi^2 - 2.182 \times 10^{-1}\phi)r$$
$$+ p + 1.941 \times 10^{-1}q + 2.772 \times 10^{-1}r$$

$$\dot{x}_{c_R} = 4.900r - x_{c_R}$$

References

[1] Heller, M., Niewoehner, R., and Lawson, P. K., "On the Validation of Safety Critical Aircraft Systems, Part I: An Overview of Analytical & Simulation Methods," *AIAA Guidance, Navigation, and Control Conference*, No. AIAA 2003-5559, 2003.

[2] Heller, M., David, R., and Holmberg, J., "Falling leaf motion suppression in the F/A-18 Hornet with revised flight control software," *AIAA Aerospace Sciences Meeting*, No. AIAA-2004-542, 2004.

[3] Chakraborty, A., Seiler, P., and Balas, G., "Susceptibility of F/A-18 Flight Control Laws to the Falling Leaf Mode Part I: Linear Analysis," *AIAA Guidance, Navigation, and Control*, 2010.

[4] Tan, W., *Nonlinear Control Analysis and Synthesis using Sum-of-Squares Programming*, Ph.D. thesis, University of California, Berkeley, 2006.

[5] Topcu, U., Packard, A., Seiler, P., and Wheeler, T., "Stability region analysis using simulations and sum-of-squares programming," *Proceedings of the American Control Conference*, 2007, pp. 6009–6014.

[6] Topcu, U., Packard, A., and Seiler, P., "Local stability analysis using simulations and sum-of-Squares programming," *Automatica*, Vol. 44, No. 10, 2008, pp. 2669–2675.

[7] Chiang, H.-D. and Thorp, J., "Stability regions of nonlinear dynamical systems: A constructive methodology," *IEEE Transactions on Automatic Control*, Vol. 34, No. 12, 1989, pp. 1229–1241.

[8] Davison, E. and Kurak, E., "A computational method for determining quadratic Lyapunov functions for nonlinear systems," *Automatica*, Vol. 7, 1971, pp. 627–636.

[9] Genesio, R., Tartaglia, M., and Vicino, A., "On the estimation of asymptotic stability regions: State of the art and new

proposals," *IEEE Transactions on Automatic Control*, Vol. 30, No. 8, 1985, pp. 747–755.

[10]Tibken, B., "Estimation of the domain of attraction for polynomial systems via LMIs," *Proceedings of the IEEE Conference on Decision and Control*, 2000, pp. 3860–3864.

[11]Tibken, B. and Fan, Y., "Computing the domain of attraction for polynomial systems via BMI optimization methods," *Proceedings of the American Control Conference*, 2006, pp. 117–122.

[12]Vannelli, A. and Vidyasagar, M., "Maximal Lyapunov functions and domains of attraction for autonomous nonlinear systems," *Automatica*, Vol. 21, No. 1, 1985, pp. 69–80.

[13]Parrilo, P., *Structured Semidefinite Programs and Semialgebraic Geometry Methods in Robustness and Optimization*, Ph.D. thesis, California Institute of Technology, 2000.

[14]Prajna, S., Papachristodoulou, A., Seiler, P., and Parrilo, P. A., *SOSTOOLS: Sum of squares optimization toolbox for MATLAB*, 2004.

[15]Jarvis-Wloszek, Z., *Lyapunov Based Analysis and Controller Synthesis for Polynomial Systems using Sum-of-Squares Optimization*, Ph.D. thesis, University of California, Berkeley, 2003.

[16]Jarvis-Wloszek, Z., Feeley, R., Tan, W., Sun, K., and Packard, A., "Some Controls Applications of Sum of Squares Programming," *Proceedings of the 42nd IEEE Conference on Decision and Control*, Vol. 5, 2003, pp. 4676–4681.

[17]Tan, W. and Packard, A., "Searching for control Lyapunov functions using sums of squares programming," *42nd Annual Allerton Conference on Communications, Control and Computing*, 2004, pp. 210–219.

[18]Jarvis-Wloszek, Z., Feeley, R., Tan, W., Sun, K., and Packard, A., *Positive Polynomials in Control*, Vol. 312 of *Lecture Notes in Control and Information Sciences*, chap. Controls Applications of Sum of Squares Programming, Springer-Verlag, 2005, pp. 3–22.

[19]Khalil, H., *Nonlinear Systems*, Prentice Hall, 2nd ed., 1996.

[20]Vidyasagar, M., *Nonlinear Systems Analysis*, Prentice Hall, 2nd ed., 1993.

[21]Hauser, J. and Lai, M., "Estimating quadratic stability domains by nonsmooth optimization," *Proceedings of the American Control Conference*, 1992, pp. 571–576.

[22]Hachicho, O. and Tibken, B., "Estimating domains of attraction of a class of nonlinear dynamical systems with LMI methods based on the theory of moments," *Proceedings of the IEEE Conference on Decision and Control*, 2002, pp. 3150–3155.

[23]Lofberg, J., "YALMIP : A Toolbox for Modeling and Optimization in MATLAB," *Proceedings of the CACSD Conference*, Taipei, Taiwan, 2004.

[24]Sturm, J., "Using SeDuMi 1.02, a MATLAB toolbox for optimization over symmetric cones," *Optimization Methods and Software*, 1999, pp. 625–653.

[25]Balas, G., Packard, A., Seiler, P., and Topcu, U., "Robustness Analysis of Nonlinear Systems," http://www.aem.umn.edu/ AerospaceControl/.

[26]Napolitano, M. R., Paris, A. C., and Seanor, B. A., "Estimation of the longitudinal aerodynamic parameters from flight data for the NASA F/A-18 HARV," *AIAA Atmospheric Flight Mechanics Conference*, No. AIAA-96-3419-CP, 1996, pp. 469–478.

[27]Napolitano, M. R., Paris, A. C., and Seanor, B. A., "Estimation of the lateral-directional aerodynamic parameters from flight data for the NASA F/A-18 HARV," *AIAA Atmospheric Flight Mechanics Conference*, No. AIAA-96-3420-CP, 1996, pp. 479–489.

[28]Lluch, C. D., *Analysis of the Out-of-Control Falling Leaf Motion using a Rotational Axis Coordinate System*, Master's thesis, Virginia Polytechnic Institue and State Unniversity, 1998.

[29]Iliff, K. W. and Wang, K.-S. C., "Extraction of lateral-directional stability and control derivatives for the basic F-18 aircraft at high angles of attack," *NASA TM-4786*, 1997.

[30]Napolitano, M. R. and Spagnuolo, J. M., "Determination of the stability and control derivatives of the NASA F/A-18 HARV using flight data," Tech. rep., NASA, 1993.

[31]Buttrill, S. B., Arbuckle, P. D., and Hoffler, K. D., "Simulation model of a twin-tail, high performance airplane," Tech. Rep. NASA TM-107601, NASA, 1992.

[32]Stengel, R., *Flight Dynamics*, Princeton University Press, 2004.

[33]Cook, M., *Flight Dynamics Principles*, Wiley, 1997.

[34]Heller, M., Niewoehner, R., and Lawson, P. K., "High angle of attack control law development and testing for the F/A-18E/F Super Hornet," *AIAA Guidance, Navigation, and Control Conference*, No. AIAA-1999-4051, 1999, pp. 541–551.

[35]Carter, B. R., *Time optimization of high performance combat maneuvers*, Master's thesis, Naval Postgraduate School, 2005.